Metallurgical and Microhardness Investigations of Ferritic Stainless Steel 409M Welds

Pradeep Khanna

Associate Professor, Department of Mechanical Engineering, NSUT, New Delhi

Email: pradeep.khanna@nsut.ac.in

ORCID: Pradeep Khanna: https://orcid.org/0000-0002-1124-5981

Crossref
Similarity Check
Powered by iThenticate

Abstract

Ferritic stainless steel 409M was MIG welded with austenitic stainless-steel wire 308L using commercially pure Argon as the shielding gas. Experiments planned were conducted using an automated welding unit for study of different aspects of the welds. One of the important aspects investigated viz. microstructural analysis in conjunction with microhardness survey is presented in this paper. Weld characteristics studied were presented on WRC-1992 diagram and Balmforth's diagram to give insight into the composition of the welds being investigated. Extensive microhardness survey covering all the three weld zones viz. weld bead, heat affected zone and base metal are presented that helped in analyzing microstructural studies carried out on the same samples. The photomicrographs and the microhardness analysis have revealed finer ferrite and martensite on the base metal side. Higher values of Cr_{eq}/Ni_{eq} and martensite start temperature along with less SFE (Staking fault energy) values resulted in the formation of increased amount of lath martensite in the fusion zone. Some typical photomicrographs and the related microhardness survey graphs are included in this paper for visual representation of the results.

Keywords: Stainless steel, metallurgical studies, microhardness survey, weld zones, lath martensite.

1.0 Introduction

Fusion welding of first generation of ferritic stainless steels poses many challenges. Firstly, there is coarsening of grains observed in the fusion and heat affected zone. Secondly, there is a reduction in toughness in the weld zone [1-2]. Thirdly, the depletion of chromium from the vicinity of HAZ is a matter of concern as it increases the susceptibility towards sensitization, which can promote the tendency of stress corrosion cracking [3-5]. Finally, a poor notch resistance may result due to the presence of intergranular martensite [6].

However, investigative studies of ferritic stainless steels have indicated that austenite potential can be increased by aiming at reducing the ferrite factor; this gives rise to the formation of martensite, resulting in a considerable grain refinement and improved toughness of the weld [7]. Formation of this martensite takes place at the expense of δ-ferrite, which is believed to be responsible for the reduction of toughness [8]. However, in order to exploit these benefits, the martensite must be a low carbon martensite. This becomes a major shortcoming in the welding of first generation ferritic stainless steels [3].

In past few years however, there has been a surge in industrial applications requiring fusion welding of these steels as they offer low cost fabricability. This demand has been addressed by the development of second generation modified ferritic stainless steels 409M, which are lean alloyed, leading to improvement in as welded HAZ properties [8]. The material finds applications in material handling equipment, coal mining, sugar, food processing, rail and road transport industries. The material combines the benefits of stainless steels and carbon steels for mechanical properties, low cost, good weldability and corrosion resistance [9]. Unlike conventional first generation ferritic stainless steels, this modified version undergoes a partial phase transformation from ferrite to austenite during cooling, the conversion of austenite to martensite upon further cooling forms grain boundary martensite which by restricting
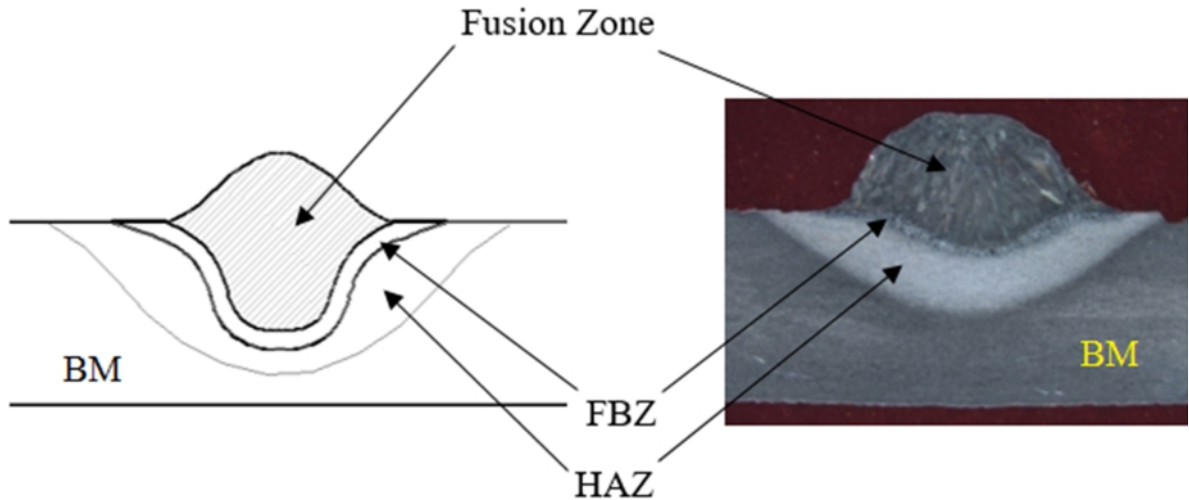
Fig. 1 : Different weld zones

the grain growth improves weldability and weld toughness [10]. Looking at the potential future of this material and availability of relatively less comprehensive investigative material from the welding viewpoint, it was felt that a detailed microstructural study of different zones of the welds viz. fusion zone (FZ), Heat affected zone (HAZ), fusion boundary zone (FBZ) and unaffected base metal (BM), in conjunction with a detailed microhardness survey can lead to a comprehensive understanding of the microstructure, which further helps to estimate the mechanical properties and service performance of the weld. **Fig. 1** shows the different zones of a weld.

When matching ferritic steel filler is used, coarse columnar grains are produced in the weld as well as heat affected zone, reducing the toughness and ductility of weld at room temperature [11]. Whereas, using austenitic stainless-steel filler wire improves the toughness, impact strength and tensile strength of the weld [12-13]. Austenitic stainless steel grade 308L gives better fatigue performance, strength and hardness over 309L and 316L [14]. Therefore, in the present work, austenitic filler 308L was used with industrially pure shielding gas Argon on a MIG welding set-up.

2.0 Experimental investigations

Table 1 and **Table 2** show the composition of stainless steel 409M and the austenitic filler metal. Weld parameters used to lay the weld beads are given in **Table 3**. Eleven numbers of welds were prepared by using bead on plate method.

Table 1 : Chemical composition of stainless steel 409M (data from supplier)

C	Si	Mn	P	S	Cr	Ni	Mo	Cu	Nb	N	Al	Ti
(%)	(%)	(%)	(%)	(%)	(%)	(%)	(%)	(%)	(%)	(%)	(%)	(%)
0.029	0.55	1.2	0.029	0.03	11.0	0.15	0.033	0.116	0.016	0.01	0.001	0.005

Table 2 : Chemical composition of filler wire 308L (data from supplier)

C	Si	Mn	P	S	Cr	Ni	Mo	Cu	Nb	N
(%)	(%)	(%)	(%)	(%)	(%)	(%)	(%)	(%)	(%)	(%)
0.020	0.50	1.70	0.012	0.03	19.00	9.00	2.60	0.08	0.025	0.051

Table 3 : Welding parameters for different specimens

Specimen	Welding Current (A)	Wire Feed rate (m/min)	Welding speed (cm/min)	Voltage (V)	Nozzle to plate distance (mm)	Torch angle (degree)
1	168	2.8	40	26	15	90
2	236	6.8	40	26	15	90
3	269	10.8	40	26	15	90
4	210	6.8	30	26	15	90
5	199	6.8	50	26	15	90
6	214	6.8	40	26	10	90
7	191	6.8	40	26	20	90
8	184	6.8	40	20	15	90
9	227	6.8	40	32	15	90
10	179	6.8	40	26	15	105
11	179	6.8	40	26	15	75

The filler wire of diameter 1.2 mm was used with commercially pure Argon gas shield at a flow rate of 15 liters per minute. Specimens were then taken out from each plate and were polished and etched using a recommended etchant for a duration of 10-15 seconds.

To estimate the chemistry of the weld, the following formula was used to calculate the percentage dilution from the weld bead geometry.

Dilution (%) = B/(A+B)   ....(1)

Where, A = area of reinforcement height

      B = area of depth of penetration

      A+B = total cross-sectional area of the bead

These areas were found graphically with the help of a planimeter.

3.0 Prediction of weld microstructures

Schaeffler diagram is generally found useful to estimate the microstructure in the FZ of stainless steels welds, but it suffers with some predictive inaccuracies as it does not take into account the effects of some elements like nitrogen, copper and niobium etc. To address this issue, many efforts have been made during past many years which have resulted in Delong's diagram, followed by WRC-1988 and very recently in the form of WRC-1992 diagrams which has further been modified to give more accurate prediction of the stainless-steel weld micro-structure [15-16].

Now the amount of heat input into the weld affects the weld dilution. To make use of the modified WRC-1992 constitution diagram, the composition of the welds were calculated from the percentage dilution, using relation (1) and presented in **Table 4**.

Table 4 : Calculated values of dilution

	Specimen Number										
	1	2	3	4	5	6	7	8	9	10	11
Dilution (%)	32.5	53.3	55.1	64.1	39	48	45	29.2	53	43.8	50.2

The calculated composition values were used to calculate Chromium and Nickel equivalents from the following equations [16], and Cr_{eq} and Ni_{eq} values are given in **Table 5.**

$$Cr_{eq} = Cr\% + Mo\% + 0.7\ Nb\% \qquad \text{......... (2)}$$

$$Ni_{eq} = Ni\% + 35\ C\% + 20\ N\% + 0.25\ Cu\% \qquad \text{........ (3)}$$

These Cr_{eq} and Ni_{eq} values are then plotted on the modified WRC-1992 diagram, to estimate the ferrite and martensite contents in the different weld compositions as shown in **Fig. 2**.

Referring to **Fig. 2**, it is evident from the minimal transverses spread of the specimens on WRC-1992 diagram, the variation in ferrite content (δ) of all the specimens is not appreciable and varies between 20 and 25.

The martensitic content however shows appreciable variations because of the significant longitudinal spread. To further substantiate the claim for the formation of ferrite and martensite in weld zone, Chromium equivalent and Nickel equivalent points were further plotted on Balmforth's ferritic-martensitic stainless-steel constitution diagram [17].

Further, Chromium and Nickel equivalents were calculated with the help of following equations [17], and plotted on Balmforth's diagram as shown in **Fig. 3**.

$$Cr_{eq} = Cr\% + 2\ Mo\% + 10\ (Al + Ti)\ \% \qquad \text{......... (4)}$$

$$Ni_{eq} = Ni\% + 35\ C\% + 20\ N\% \qquad \text{......... (5)}$$

Table 5 : Dilution based composition of specimen, Cr_{eq}, Ni_{eq}, Cr_{eq} /Ni_{eq}, M_s, SFE & heat input

| Elements	Specimen Number										
	1	2	3	4	5	6	7	8	9	10	11
C	0.023	0.021	0.022	0.023	0.02	0.021	0.022	0.019	0.022	0.021	0.022
Si	0.516	0.522	0.527	0.532	0.519	0.524	0.527	0.514	0.526	0.522	0.525
Mn	1.537	1.473	1.425	1.380	1.505	1.460	1.425	1.555	1.435	1.480	1.450
P	0.017	0.019	0.021	0.022	0.018	0.020	0.021	0.016	0.021	0.019	0.020
S	0.028	0.028	0.029	0.029	0.028	0.028	0.029	0.028	0.029	0.028	0.029
Cr	16.40	15.37	14.60	13.88	15.88	15.16	14.60	`16.6	14.76	15.48	15.00
Ni	6.123	4.990	4.132	3.336	5.548	4.752	4.132	6.433	4.309	5.106	4.575
Mo	0.088	0.028	0.069	0.062	0.083	0.075	0.069	0.091	0.055	0.078	0.074
Cu	0.091	0.096	0.099	0.102	0.094	0.097	0.099	0.090	0.099	0.095	0.098
Nb	0.022	0.020	0.020	0.019	0.021	0.019	0.020	0.022	0.020	0.021	0.020
N	0.037	0.032	0.028	0.024	0.035	0.031	0.028	0.039	0.029	0.032	0.030
Al	0.003	0.005	0.005	0.006	0.004	0.005	0.005	0.003	0.005	0.004	0.005
Ti	0.002	0.003	0.003	0.003	0.002	0.002	0.002	0.001	0.003	0.002	0.003
Cr_{eq}	16.5	15.41	14.68	13.95	15.97	15.24	14.68	16.78	14.82	15.57	15.08
Ni_{eq}	6.95	6.4	5.48	4.64	6.96	6.12	5.48	7.89	5.67	6.49	5.96
Cr_{eq}/Ni_{eq}	2.37	2.4	2.67	3.00	2.29	2.49	2.66	2.12	2.61	2.39	2.53
Ms (°C)	56.7	73.38	130.21	172.61	45.88	85.56	129.77	11.89	121.07	70.76	87.17
SFE (mJ/m²)	8.32	7.18	3.46	1.02	8.53	6.12	3.16	8.96	3.87	7.54	5.21
Heat Input (kJ/mm)	0.654	0.919	1.048	1.092	0.620	0.834	0.744	0.551	1.089	0.697	0.697
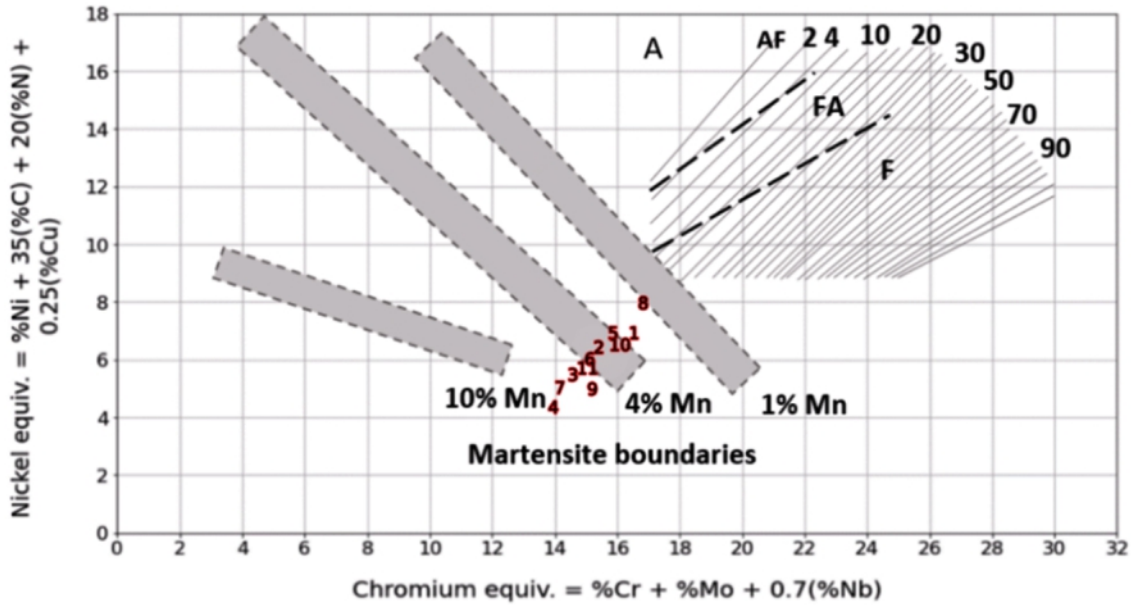
Fig. 2 : Position of different weld specimens on a WRC-1992 diagram [8].

From **Fig. 3**, it is evident that all points are falling in the martensite-ferrite region. This can further be validated for different specimens with different heat inputs by calculating the martensite start temperature for all the specimens by using following relation [8].

$$MS\ (°C) = 526 - 12.5\ Cr - 17.4\ Ni - 29.7\ Mn - 31.7\ Si - 354\ C - 20.8\ Mo - 1.34\ (Cr+\ Ni) + 22.4\ (Cr+Mo)\ C \qquad .... (6)$$
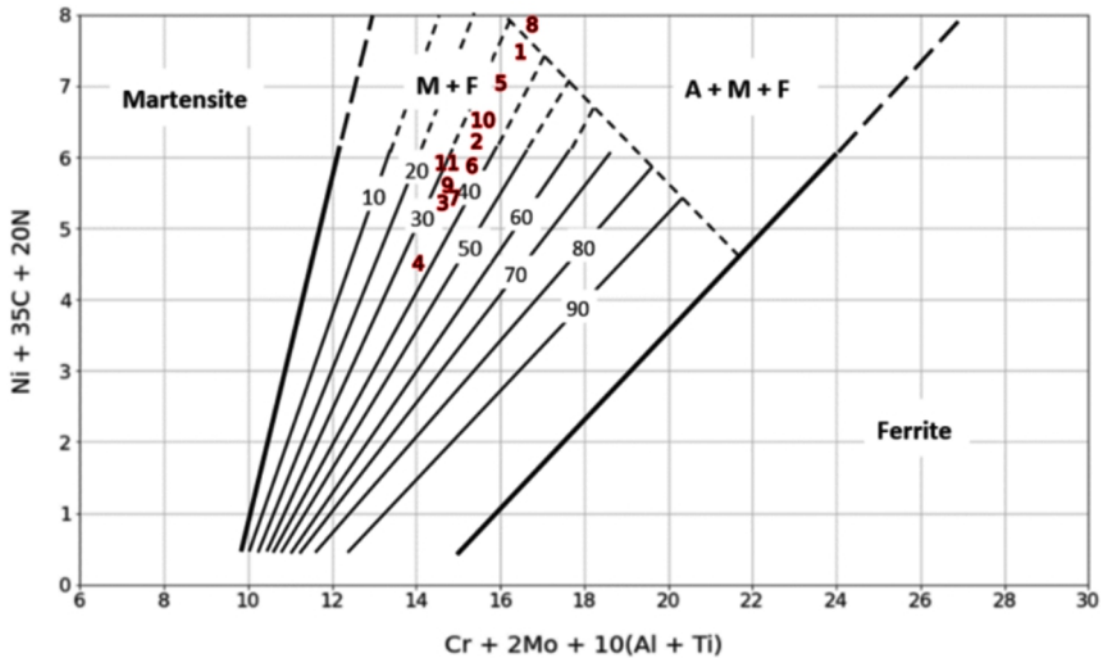
Fig. 3 : Position of different weld specimen on Balmforth's diagram [17].

The calculated values of martensite start temperature for different specimens are presented in **Table 5**. It can be observed that martensite start temperature increases with increase in Cr_{eq}/Ni_{eq} ratio as shown in **Fig. 4**. Thereby creating a kind of correlation between the two and it can be inferred that the variation in composition in different weld specimens owing to different welding conditions has caused difference in martensite start temperature hence the amount of martensite laths. Again, the welds with higher heat inputs have more martensite laths formed because of higher Cr_{eq}/Ni_{eq} ratio and more martensite start temperature. It is evident from **Fig. 2**, that specimen 4 with largest heat input has maximum value of martensite start temperature and hence maximum martensite laths, whereas specimen 8 with least heat input has minimum martensite start temperature and hence minimum amount of martensite laths.

Furthermore, the transformation of various microstructural phases and straining of the material during welding alters the staking fault energy (SFE) of the weld microstructure [18]. Therefore, estimation of SFE of different weld specimens can also help in the prediction of weld microstructure. The SFE for the weld specimens at hand were estimated by the following equation [19].

$$SFE = 1.2 + 1.4\ Ni\% + 0.6\ Cr\% + 7.7\ Mn\% - 44.7\ Si\% \qquad \text{............... (7)}$$

The calculated values of SFE for different weld specimens are given in **Table 5**. Again, it can be seen that SFE and heat input have inverse relation. Therefore, specimen 4 with largest heat input has minimum value of SFE, whereas specimen 8 with least heat input has maximum value of SFE. Now, martensitic transformation is favored by a low value of SFE [20]. In the
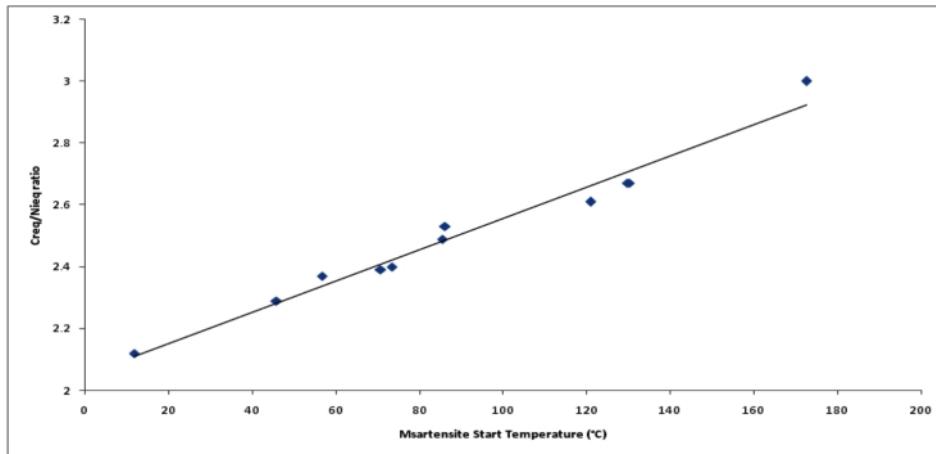

Fig. 4 : Variation in Cr_{eq}/Ni_{eq} with respect to martensite start temperature
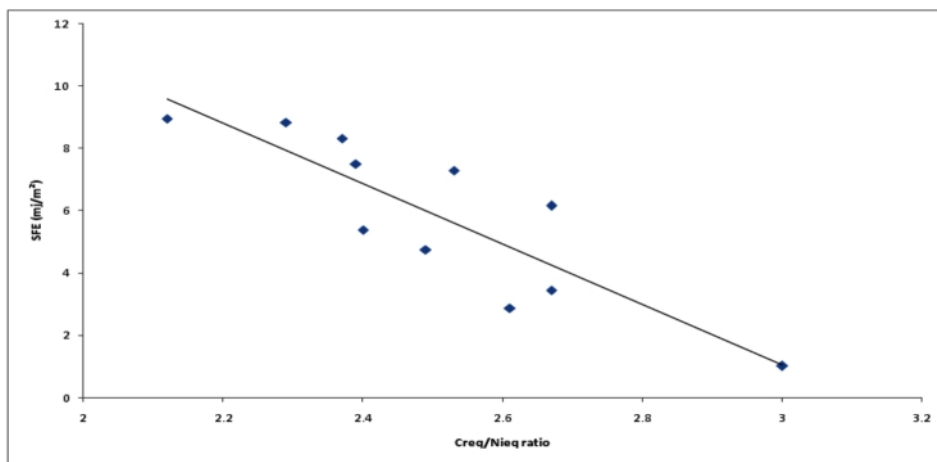

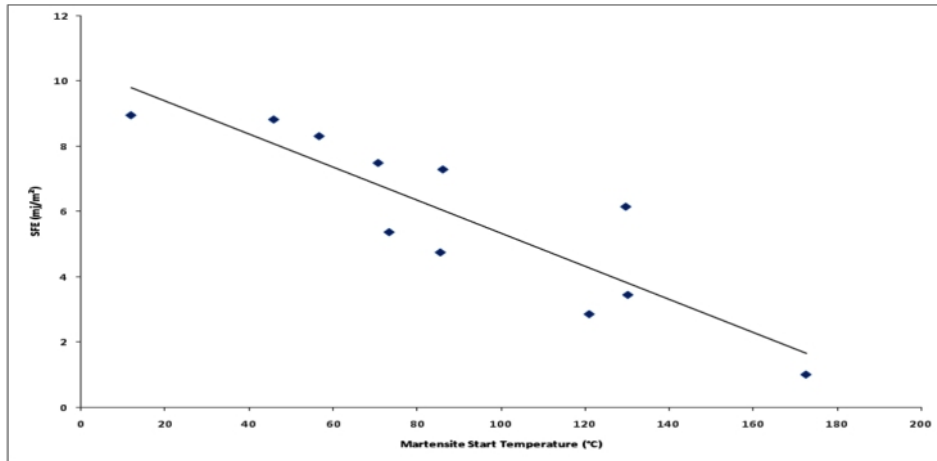Fig. 5 : Variation in SFE with respect to Cr_{eq}/Ni_{eq}

Fig. 6 : Variation in SFE with respect to martensite start temperature

Sample 1 : (0.654 kJ/mm)

Sample 2 : (0.919 kJ/mm)

Sample 3 : (1.048 kJ/mm)

Sample 4 : (1.092 kJ/mm)

Sample 5 : (0.620 kJ/mm)

Sample 6 : (0.834 kJ/mm)

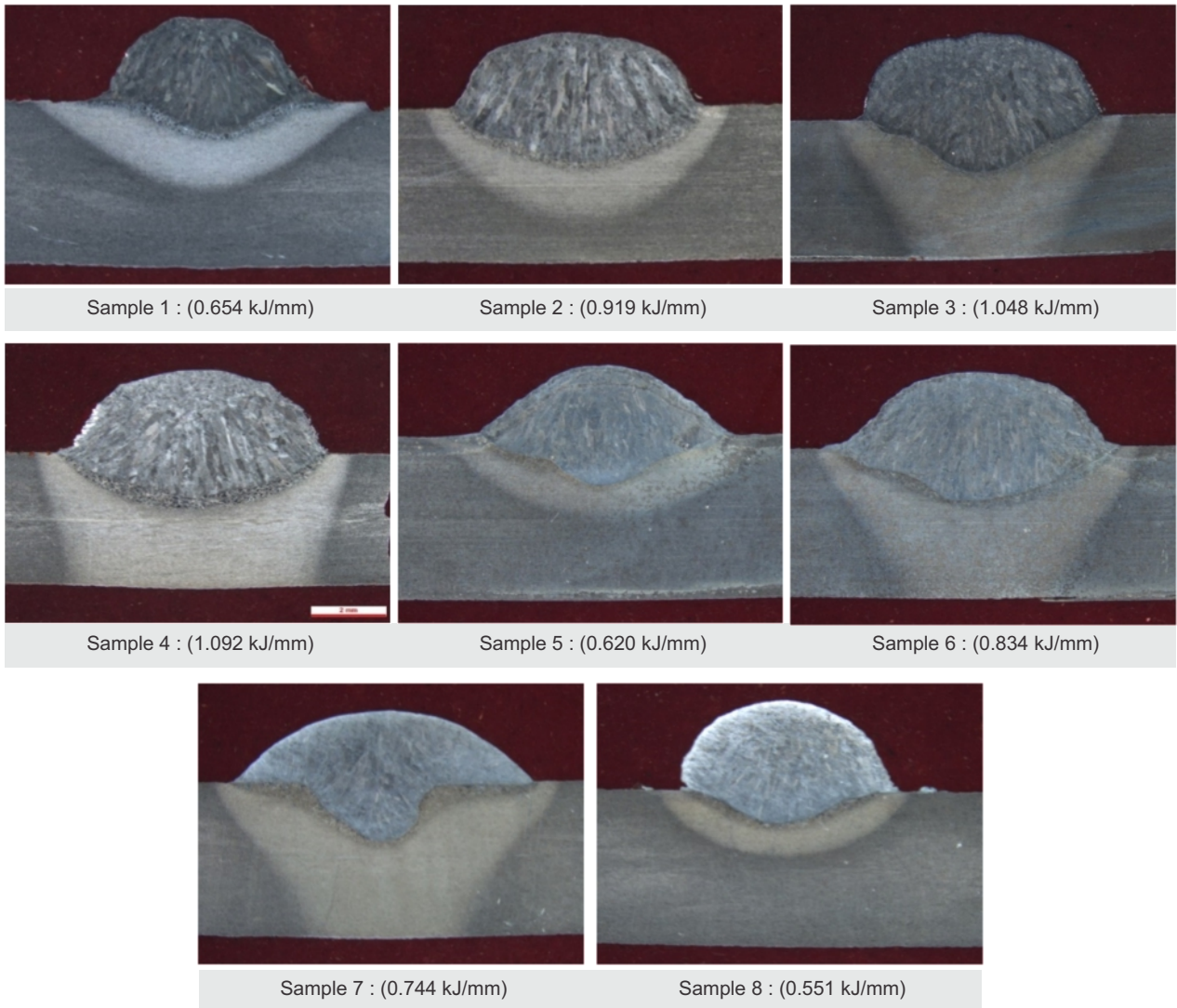Sample 7 : (0.744 kJ/mm)

Sample 8 : (0.551 kJ/mm)

Fig. 7 : Macrographs of weld samples at different heat inputs

present work, therefore it is expected that for weld specimens with SFE less than 9 mJ/m², more amount of austenite will transform to lath martensite. Consequently, SFE can be correlated with Cr_{eq} /Ni_{eq} ratio in a way that both are related inversely. Similar relation of SFE exists with martensite start temperature, as shown in **Fig. 5** and **Fig. 6** respectively. Therefore, a higher value of SFE favors the stability of austenite and restricts the formation of martensite by lowering its MS temperature. In all weld specimens, the SFE is less than 9 mJ/m²; therefore, transformation of austenite into lath martensite is inevitable in these welds.

The macrographs at low resolution (10X) of some of the weld specimens are shown in **Fig. 7**, showing the impact of heat input on the size of different weld zones. It can be seen that with the increase in heat input, the depth of penetration, width and HAZ increased. The micrographs of the weld metal reveal the presence of dendritic grains of coarse ferrite, austenite and relatively finer martensite laths. The distribution of phases is non-uniform as it is the weld zone, **Fig. 8**.

This mix of microstructures is obtained probably because the weld has been made between ferritic base metal and an austenitic filler wire. Cr_{eq} /Ni_{eq} ratio is found to have a major impact on the formation of ferrite (δ). It is reported that when the Cr_{eq} /Ni_{eq} ratio is less than 1.35, formation of austenite during solidification is favored, whereas a Cr_{eq} /Ni_{eq} ratio more than 1.35 results in the formation of ferrite during solidification. It is clear from **Table 5**, that all the weld specimens have Cr_{eq} /Ni_{eq} ratio more than 1.35, therefore all the welds have solidified in ferrite-austenite solidification mode [21].

This mode can further be explained by diagram shown in **Fig. 9**, where all the weld metals lie in two phases (δ+γ) solidification zone, as evident from the location of specimen 4 with highest heat input and specimen 8 with lowest heat input on this diagram. The higher martensite content in the welds produced with higher heat inputs can be explained by taking into account the manner of transformation of δ-ferrite into austenite. In addition, an increase in the Cr_{eq} /Ni_{eq} ratio and MS temperature results in reduced stability of austenite consequently increasing the tendency to transform into martensite on cooling.

Fig. 10 shows the photomicrographs of different specimen under high resolution. The effect of heat input on the microstructure is quite visible. The microstructure obtained in the HAZ is shown in **Fig. 11**. The HAZ shows coarse ferrite grains and martensite laths. The reason for the formation of martensite from the metastable austenite can be due to fast cooling rates during welding. The volume % of martensite is around 45% and ferrite around 55%. The ferrite is more fine and martensite is more columnar on the base metal side whereas coarser ferrites and finer martensite on the weld side.

Comparing **Fig. 8** and **Fig. 11**, it can easily be seen that the weld metal fusion zone attributes to finer grains as compared to HAZ grains, irrespective to the amount of heat input.
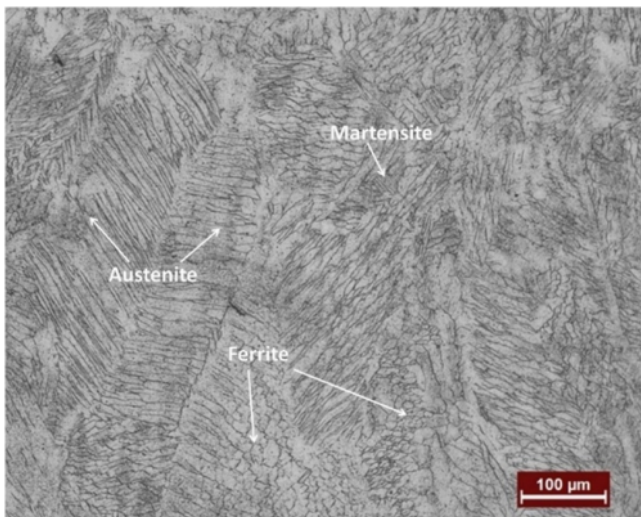

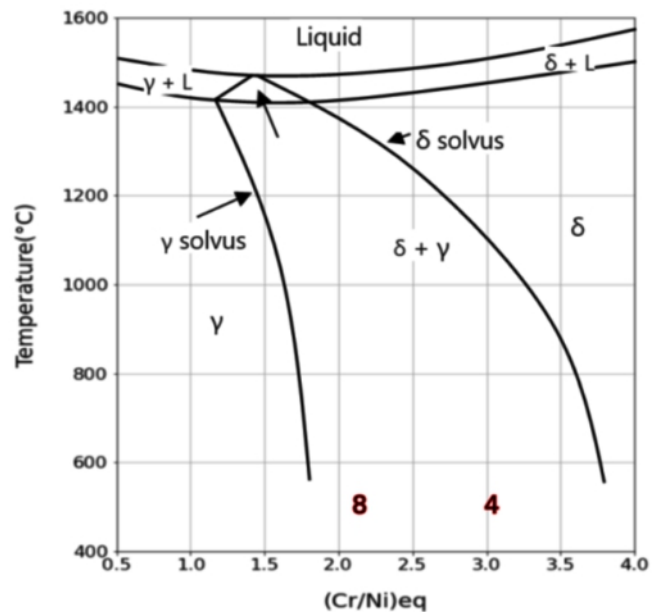Fig. 8 : Microstructure of the fusion zone
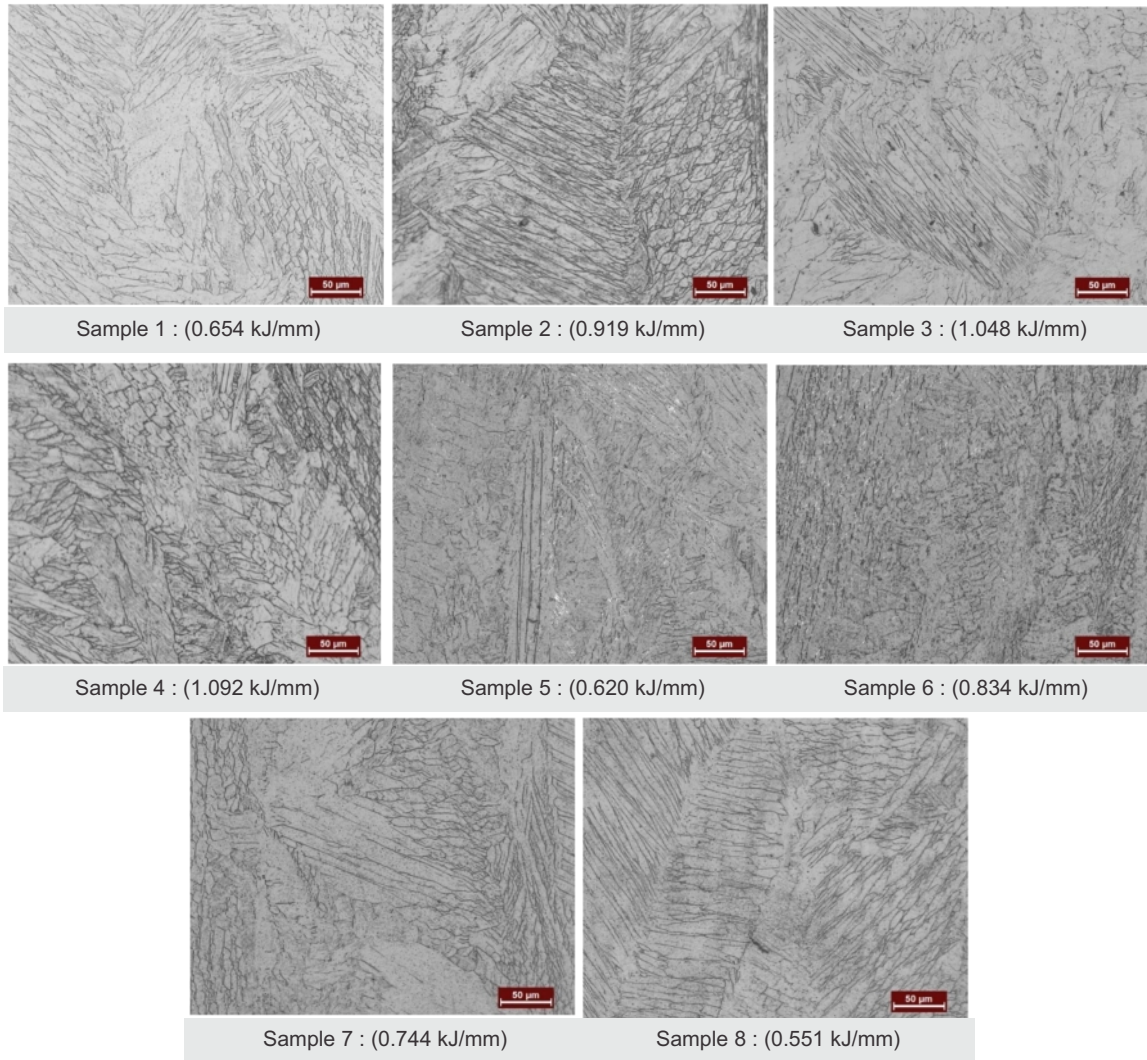

Fig. 9 : Pseudo-binary phase diagram [20].

Sample 1 : (0.654 kJ/mm)	Sample 2 : (0.919 kJ/mm)	Sample 3 : (1.048 kJ/mm)
Sample 4 : (1.092 kJ/mm)	Sample 5 : (0.620 kJ/mm)	Sample 6 : (0.834 kJ/mm)
Sample 7 : (0.744 kJ/mm)	Sample 8 : (0.551 kJ/mm)	

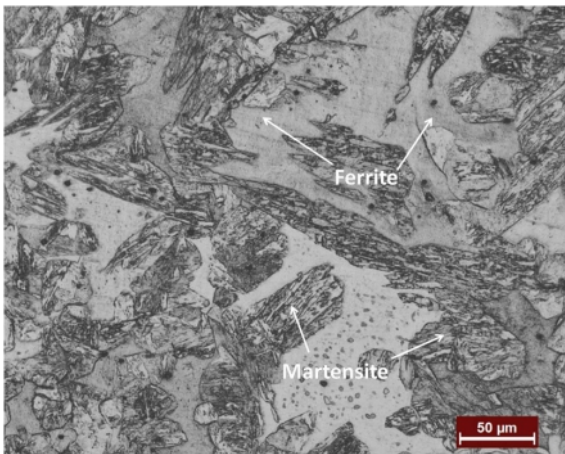Fig. 10 : Micrographs of weld samples at different heat inputs

Fig. 11 : Heat affected zone

Fig. 12 shows that the weld with higher heat inputs resulted in the higher amount of martensite than weld at lower heat input. However, the amount of martensite is so less that it cannot restrict the grain growth as it did in the fusion zone. Thus, the welds with higher heat inputs tend to have coarse grains. The martensite laths are also present in the HAZ; however, this amount is less than the amount in FZ.

Fig. 13 shows weld FZ, HAZ and unaffected BM together for better understanding. The unaffected base metal shows a ferritic structure with equiaxed grain morphology with a grain size of around 25 μm and is shown in **Fig. 14**.

4.0 Microhardness Survey

Metallurgical investigations are almost invariably supplemented by microhardness survey of different zones of the

71
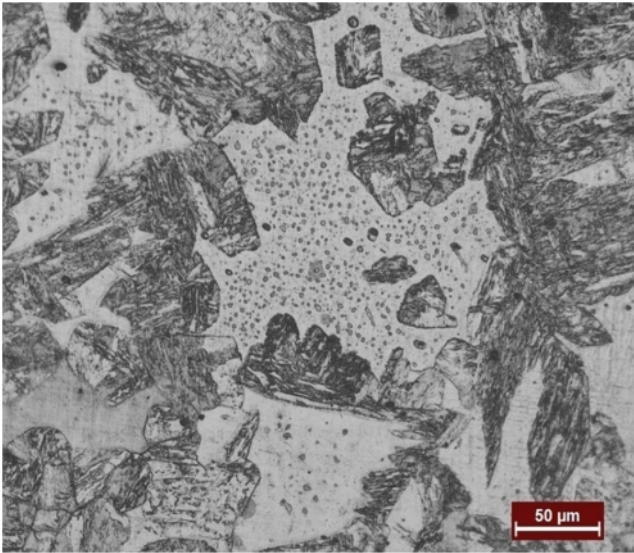
Sample 4 : (1.092 kJ/mm)
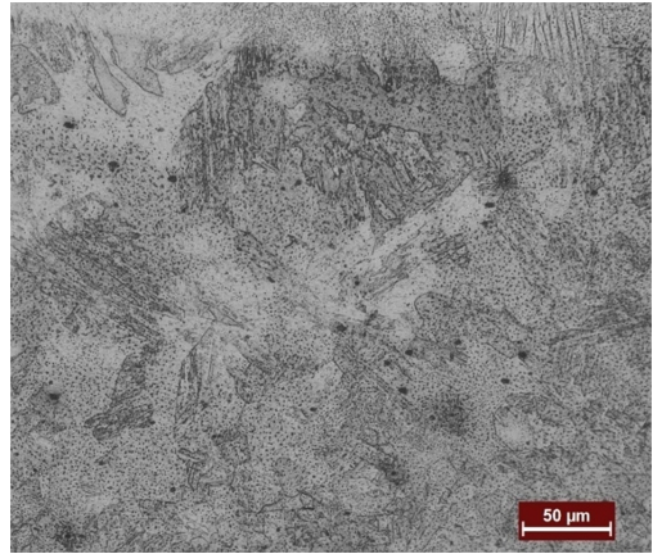
Sample 8 : (0.551 kJ/mm)

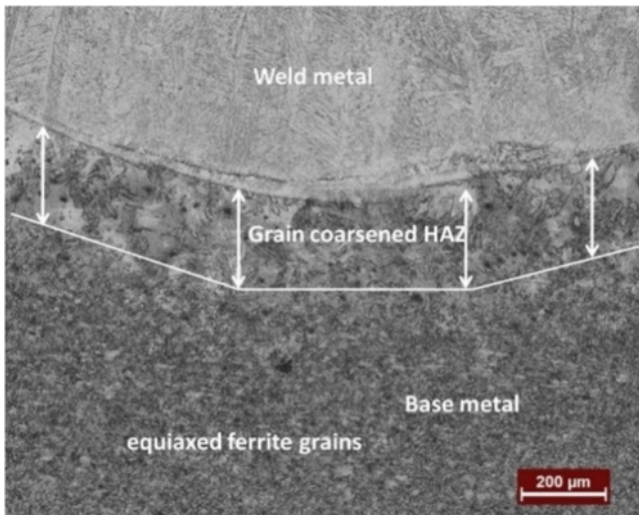Fig. 12 : Comparison of HAZ grain sizes at different heat inputs
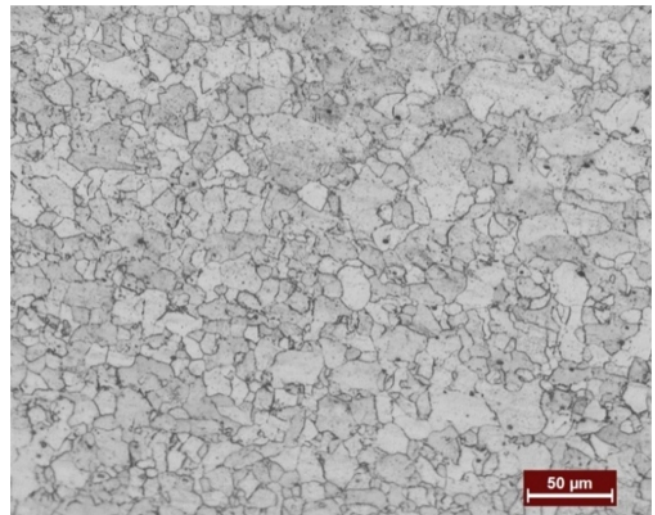

Fig. 13 : FZ, HAZ and unaffected base metal

Fig. 14 : Base metal with equiaxed ferrite grains

weldment to corroborate the nature of microstructure constituents by differentiating one transformation product from the other in different zones on the basis of their hardness values.

MIG welding is a high cooling rate process where the heating and cooling are so fast that it is not always possible to predict as to what extent a particular phase transformation has taken place. Because of differential cooling rates at different points, the consequent phase transformations will be different, giving rise to a complex microstructure [22]. Therefore, in order to differentiate one transformation from the other, microhardness survey of different zones of interest is carried out.

The weld specimens used for carrying out metallurgical investigations were only used for microhardness survey. The scheme could well be considered as based on heat input rates. The microhardness value of the parent metal was determined (as per ASTM E834) separately and was superimposed on the graphs depicting the microhardness values for fusion zone, fusion boundary zone and heat affected zone. Microhardness values of all the samples were measured by using Vickers microhardness tester of make 'Future Tech', model FM-700e, under a load of 50 gm and the attached microscope was having
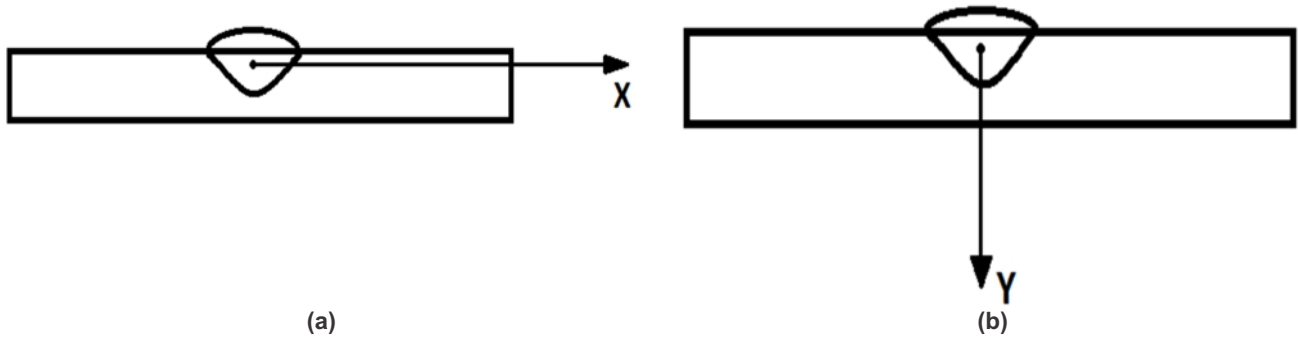
(a)　　　　　　　　　　　　　　　　　　　　　　　(b)

Fig. 15 : Microhardness along horizontal and vertical axis

a magnification of X300. The hardness values were measured in two directions, one along the horizontal axis and the other along vertical axis, starting from the centre of the bead towards HAZ. The arrangement is presented in **Fig. 15(a,b)**. The results were graphically plotted to clearly understand the effect of different weld parameters on microhardness values in various weld zones.

5.0　Results of microhardness survey

The results in the form of microhardness graphs were then plotted for all the specimens. In order to keep the content within reasonable limits, only a few of these are being discussed and are presented in **Fig. 16** and **Fig. 17**. Each of these figures has two parts (a) and (b). Part (a) represents the microhardness values along the vertical axis of the weld bead and part (b) shows microhardness values along the horizontal axis. Microhardness values of the parent metal have been

superimposed in each figure for comparison.

5.1　Analysis of results

The graphical results are analysed to understand the effects of various welding parameters on the microhardness values in different zones as given below;

All the graphs indicate a common trend, that is, the hardness value of fusion zone is maximum, followed by that of the HAZ and finally the BM having the lowest value. This could be because of finer martensitic laths in the fusion zone, coarser martensitic structure in HAZ and equiaxed ferritic grains in the base metal. **Fig. 16(a,b)** show the effect of wire feed rate, along the vertical and horizontal axes of the weld. It shows that the microhardness was much higher in the FZ and kept dropping in the HAZ to nearly the same value as that of parent metal. The reason could be attributed to the fact that the ferrite is finer and martensite is more columnar on the base
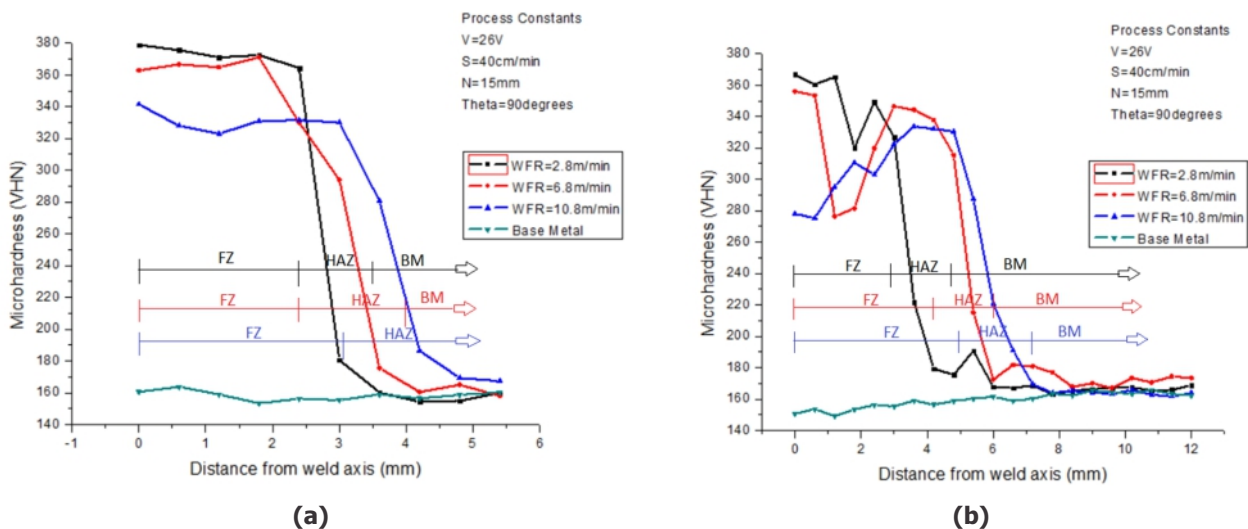

(a)　　　　　　　　　　　　　　　　　　　　　　　(b)

Fig. 16 (a,b) : Effect of WFR on microhardness along vertical & horizontal axes.
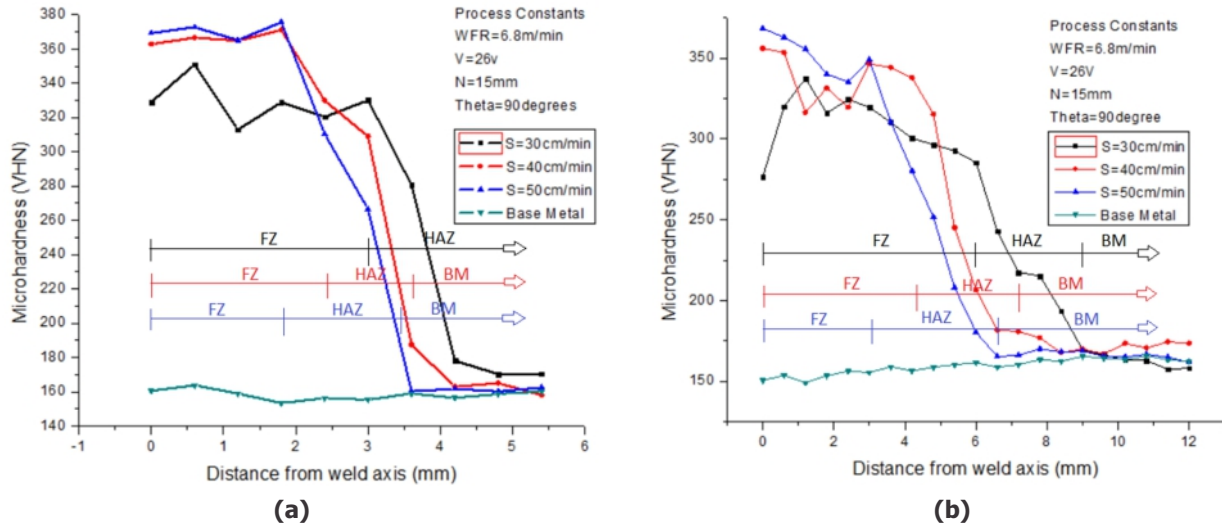
Fig. 17 (a,b) : Effect of welding speed on microhardness along vertical & horizontal axis

metal side having lower hardness values, whereas coarser ferrites and finer martensite are on the weld side having higher hardness values. The wire feed rate of 2.8 m/min consistently showed higher values than at 6.8 m/min and 10.8 m/min in the fusion zone. The reason may be that at lower values of WFR, the cooling rate is faster, which contributes to the higher hardness values [23].

Further, **Fig. 16(a)** also shows that at wire feed rate of 10.8 m/min, the heat affected zone has almost extended till the complete thickness of the specimen. The probable explanation could be that with more wire feed rates (WFR), the heat was so intense that it penetrated to almost complete depth of the specimen.

Similarly, **Fig. 17(a,b)** show the microhardness values along the vertical and horizontal axis of the weld respectively. Microhardness is maximum at a welding speed of 50 cm/min, which is indicative of the fact that at higher welding speeds due to faster cooling rates, a hard microstructure is formed. **Fig. 17(a)** shows that at welding speed of 30 cm/min, the heat affected zone has almost extended till the complete thickness of the specimen. The reason could be that at slower welding speeds the heat input is more and it penetrated to almost complete depth of the specimen, thereby extending the HAZ.

Further, **Fig. 17(b)** depicts that the FZ width is maximum in case of welding speed 30 cm/min. this could be because at slower welding speeds, the heat going to the weld is more which resulted in more melting of base metal causing it to spread more width-wise, thereby increasing the width of the fusion zone.

In the similar manner the microhardness graphs representing the effects of variables can be explained.

6.0 Conclusions

1. The weld metal reveals the presence of equiaxed ferrite and dendritic austenite and martensite laths. The distribution of phases is non-uniform as it the weld zone. The presence of ferrite and martensite can well be predicted by using modified WRC-1992 diagram and Balmforth's phase diagram.

2. Higher values of Cr_{eq} /Ni_{eq} and martensite start temperature along with less SFE values resulted in more martensite laths in the FZ.

3. Weld specimen with slower cooling rates formed more martensite as resulted from austenite (metastable) formed because of slower cooling rates.

4. The ferrite was more fine and martensite more columnar on the base metal side i.e. low temperature heat affected zone. Whereas, coarser ferrites and finer martensite was formed on the weld side i.e. high temperature HAZ.

5. The hardness of FZ was maximum, followed by HAZ and unaffected BM. Microhardness was reduced in HAZ probably due to grain growth.

6. The microstructures estimated by using different standard formulae were confirmed by the results of optical microscopy.

7. The input of heat and the rate of cooling decide the kind of microstructure formed and resulting microhardness at a given point. Microhardness varied with variations in weld parameters.

8. Microhardness was maximum at minimum WFR, maximum welding speed, minimum V, minimum NPD and maximum θ.

References

1. Reddy GM and Meshran SD (2006); Grain refinement in ferritic stainless weld through magnetic and oscillations and its effects on tensile properties. Indian Welding Journal, 39 (3), pp.35-41.

2. Reddy GM and Mohandas T (2001); Explorative studies on grain refinement of ferritic stainless-steel welds. Journal of Material Science, 20 (8), pp.722-723.

3. Amuda MOH and Mridha S (2011); An overview of sensitization dynamics in ferritic stainless-steel welds. International Journal of Corrosion, pp.1-9.

4. Mathews LM, Griesel B and Longman PT (1999) Sensitization in low carbon 12% chromium containing stainless steel. Proceedings 14th International Corrosion Congress, Cape Town, South Africa, pp.332-340.

5. Nishimura R (1992); Stress corrosion cracking of type 430 ferritic stainless steel in chloride and sulphate solutions. Journal of Corrosion, 48 (11), pp.882-890.

6. Warmelo MNV (2007); Susceptibility of 12% Cr steel to sensitization during welding of thick gauge plate. M.S Thesis, University of Wollongong, Australia.

7. Marshal AW and Famar JCM (2000); Welding of ferritic and martensitic 11-14% Cr steels. International Institute of Welding document, IXH-494-200, pp.1-39.

8. Lippold JC and Kotecki DJ (2005); Welding metallurgy and weldability of stainless steels. John Wiley & Sons, Inc. New Jersey.

9. Lippold JC (2015) Welding metallurgy and weldability. John Wiley & Sons, Inc. New Jersey.

10. Sampath PS, Manimaran V and Gopinath A (2015) Wear and corrosion studies on ferritic stainless steel (SS409M). International Journal of Research in Engineering and Technology, 4 (4), pp.502-511.

11. Mukherjee M and Pal TK (2012); Influence of mode of metal transfer on microstructure and mechanical properties of gas metal arc welded modified ferritic stainless steel. Metals and Materials Transactions, 43 (6), pp.1791-1808.

12. Taban E, Deleu E and Dhooge A (2008); Submerged arc welding of thick ferritic martensitic 12 Cr stainless steel with a variety of consumables. Journal of Science and Technology of Welding and Joining, 13 (4), pp.327-334.

13. Shanmugam K, Laxminarayanan AK and Balasubramaniun B (2000). Tensile and impact properties of shielded metal arc welded AISI 409M ferritc stainless steel joints. Journal of Materials Science and Technology, 25 (2), pp.181-186.

14. Mukherjee M, Saha J and Kanjilal P (2015); Influence of gas mixtures in GMAW of modified 409M ferritic stainless steel. Supplement Welding Journal, 94, pp.101s-114s.

15. Kotecki DJ and Siewart TA (1992); WRC-1992 Constitution diagram for stainless steel weld metals: a modification of WRC-1988 diagram. Welding Journal, 71 (5), pp.171s-178s.

16. Kotecki DJ (1999); A martensite boundary on the WRC-1992 diagram. Welding Research Supplement, pp.180s-192s.

17. Balmforth MC and Lippold JC (2000); A new ferritic-martensitic stainless-steel constitution diagram. Welding Journal supplement, 79 (12), pp.339s – 345s.

18. Allain S, Chateau JP and Bouaziz O (2004); Correlations between the calculated staking fault energy and the plasticity mechanisms in Fe-Mn-C alloys. Journal of Material Science and Engineering, 158, pp.387-389.

19. Rhodes C G and Thompson AW (1977); The composition dependence of staking fault energy in austenitic stainless steels. Metals and Materials Transactions, 8 (12), pp.1901-1906.

20. Tavares SSM and Pardal JM (2014); Martensitic transformation induced by cold deformation of lean duplex stainless steel. Journal of Materials Research, 17 (2), pp.381-385.

21. David SA, Vitek JM and Hebble TL (1987); Effect of rapid solidification on stainless steel weld metal microstructures and its implications on the Schaeffler Diagram. Supplement Welding Journal, 66, pp.289s-300s.

22. Kurt HI and Samur R (2013); Study on microstructure, tensile strength and hardness of stainless steel 316 joined by TIG welding. International Journal of Advancements in Engineering Science and Technology, 3 (1), pp.1-6.

23. Khanna P and Maheshwari S (2017); Microhardness analysis in MIG welding of stainless steel 409M. Journal of Production Engineering, 20 (1), pp.93 - 96.